Hollow-Shell Implosion Studies on the 60-Beam, UV OMEGA Laser System

Direct-drive inertial confinement laser fusion is accomplished by uniformly illuminating spherical fuel-bearing targets with high-power laser beams, ablatively driving implosions that result in large increases in density and temperature. Current large laser systems such as the University of Rochester's OMEGA laser, which is capable of both direct- and indirect-drive implosion experiments,[1,2] and the Lawrence Livermore National Laboratory's Nova laser,[3,4] which is designed primarily for indirect-drive implosions, are smaller in size and total output energy than what is believed necessary to obtain ignition and gain. Attaining conditions for ignition to occur (densities of ~200 g/cm^3 and temperatures of ~3 to 4 keV) awaits the completion of the National Ignition Facility[5] (NIF) and other megajoule-class drivers currently being planned. In addition to the high temperatures and densities, ignition requires fuel areal densities (density–radius product) $\gtrsim 0.3$ g/cm^2 to stop the 3.5-MeV alpha particles in order to obtain thermonuclear burn propagation.[6,7] To reach these conditions in direct-drive implosions requires controlling the growth of the Rayleigh–Taylor (RT) instability, which is seeded by nonuniformities in the laser illumination. The RT instability can lead to shell breakup and mixing of shell material into the gas-fill or central voided region in the case of evacuated targets. We are currently studying the attainment of near-ignition-scale areal densities on OMEGA and the effects of beam smoothing and pulse shaping thereon, by using surrogate cryogenic targets where the shell acts as the fuel layer. These will be followed by actual cryogenic (DD or DT) targets, when the cryogenic target–handling facility is completed.

Previously reported direct-drive OMEGA experiments have demonstrated the ability to achieve high relative temperatures[8] (kT_e ~3 to 4 keV, kT_i ~14 keV) attaining DT neutron yields of $>10^{14}$. Additionally, the acceleration- and deceleration-phase target stability has been studied in spherical implosions using thin polymer layers containing various high-Z elements, such as Ti, Cl, and Si, with D_2 fills containing a small Ar component.[9]

In the present experiments, we have studied the stagnation phase (maximum density and temperature conditions) of the implosions designed to attain high areal densities ($\gtrsim 0.1$ g/cm^3) using both x-ray and neutron spectroscopic techniques. The targets consist of both deuterated and undeuterated polymer shells with either zero-pressure (evacuated) or low-pressure (3-atm) D_2 or D^3He fills. The zero-pressure- or low-pressure-fill targets are "surrogates" for cryogenic targets since in actual cryogenic targets the gas pressure will be at or below the triple-point vapor pressure of D_2 or DT gas (0.2 atm at 20 K).[10] An equivalent particle density is obtained for a pressure of 3 atm at room temperature (300 K). The hydrodynamics of the central gas-filled region of a 3-atm-filled target will therefore be the same as an actual cryogenic target at the triple point. Conversely, the shell of the surrogate cryogenic target is not expected to evolve the same but will have a different in-flight aspect ratio (mean radius/thickness) and convergence ratio (initial radius/final radius). Also, the RT growth in a CH shell will be larger than for a DT shell because the reduced ablation velocity leads to a lesser ablative stabilization. Nevertheless, high areal densities ($\gtrsim 0.1$ g/cm^2), high convergence ratios (>20), and moderately high central temperatures ($\gtrsim 2$ keV) can be studied with a surrogate cryogenic target. The measurements described in this work have revealed significant information about the implosion of surrogate cryogenic targets and the effects of beam smoothing and pulse shaping thereon.

Experiments

The targets used for these experiments were manufactured by General Atomics.[11] Hollow spherical shells were produced by coating layers of deuterated plastic (CD) and then undeuterated plastic (CH) over a depolymerizable spherical mandrel. The coatings were accomplished by the method of glow discharge plasma (GDP) polymerization. The CD-layer thicknesses ranged from 5 to 10 μm, while the CH-layer thicknesses ranged from 10 to 30 μm. Layer thicknesses were measured to an accuracy of 0.5 μm, and the target diameter was measured to an accuracy of 1 μm. In each case the targets were

held in place in the target chamber using low-mass stalks consisting of a short length of spider silk (~100 μm) that had been previously overcoated with parylene to add mechanical stability. The spider silks were glued to boron fibers ~20 μm in diameter, and the parylene-overcoated stalk end was attached to the target with UV-curable epoxy. The UV epoxy glue spots were the largest single mass perturbation introduced by the stalks; these spots ranged from 10 to 30 μm in diameter. Targets were either prepared and kept evacuated ($<10^{-3}$ Torr) or filled with 3 atm of D_2, H_2, or an equal molar mixture of D^3He gases.

Three laser-irradiation conditions were used for these experiments: (1) Coherent beam illumination (no beam smoothing) was used with the beams focused so as to nearly tangentially illuminate the target at the beam edge. (2) Each beam was modified using a distributed phase plate (DPP)[12] at best focus (diffraction minimum spot ~0.95 mm). (3) Beams with DPP's were smoothed using SSD[13] along two axes (2-D SSD)[12] with frequencies of 3.5 and 3.0 GHz and bandwidths of 1.7 and 1.2 Å (0.25-THz bandwidth). The estimated illumination uniformity for 60 overlapping OMEGA beams (σ_{rms} for ℓ-modes 1 to 500) was ~15% for the coherent beam illumination, ~20% for DPP-only illumination, and ~2.5% for the DPP+SSD illumination. All values quoted are calculated from the idealized effect on the beam distribution and averaged over the length of the pulse. While the distributed phase plates produce a smooth envelope to the beam, they also introduce small-scale laser speckle, hence the larger value of σ_{rms} for the DPP-only illumination. Although the value of σ_{rms} for the DPP+SSD illumination is lower than the other cases, two additional effects not accounted for by this time-averaged quantity must be considered: (1) Beam balance at current levels (~7% rms

beam-to-beam energy variation) would produce an on-target illumination nonuniformity of ~2.5% rms even with perfectly smooth beams, with most of that contribution in modes 1 through 5. (2) The smoothing time of the present level of SSD may not be fast enough to avoid imprinting laser-beam speckle onto the target.

The three pulse shapes used in these experiments (Fig. 78.23) were the 1-ns square pulse shape, the 1:6 ratio foot-to-main-pulse shape (also known as PS26), and the 1:40 ratio pulse shape known as $\alpha = 3$. Examples of the actual pulse shapes are shown along with the design shape. Good pulse-shape repeatability was obtained. The purpose of varying the pulse shape in these experiments is to investigate target performance versus pulse shape. Ideally a gradually rising intensity, if properly designed, will produce a final target compression greater than a sharply rising pulse. Figures 78.24(a) and 78.24(b) show the calculated primary neutron yield (D-D) and the fuel and shell areal densities as a function of time for the three different pulse shapes. All simulations (accomplished with the hydrodynamics code *LILAC* as described in the next section) are for an assumed total energy on target of 25 kJ, and in each case the target was a 0.95-mm-diam, 20-μm-thick CH shell filled with 3 atm of D^3He. For these conditions it is clear that the highest yield and compression are obtained for the highest-contrast pulse shape. This trend also holds for the evacuated targets.

The two instruments used to obtain x-ray spectra of the implosion cores were a Kirkpatrick-Baez–type (KB) microscope outfitted with a diffraction grating[14] and a crystal spectrometer outfitted with an imaging slit.[15] The KB microscope has Ir-coated mirrors and a sensitive energy band from ~2 to
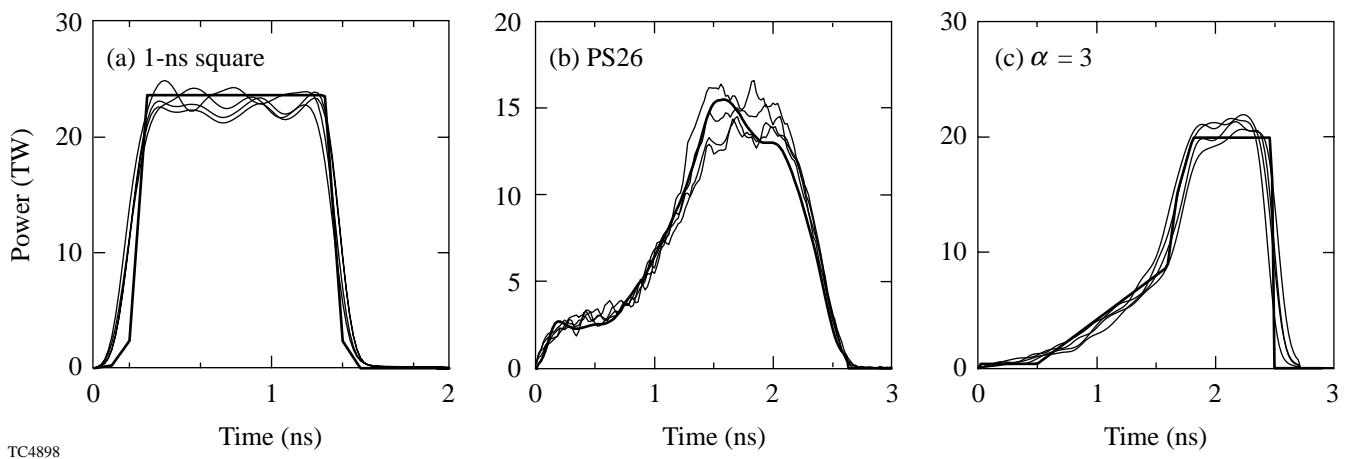

TC4898

Figure 78.23
The three pulse shapes used in these experiments: (a) the 1-ns square pulse, (b) PS26, a 1:6 ratio foot-to-main pulse shape, and (c) $\alpha = 3$, a 1:40 ratio pulse shape.

8 keV. The absolute response of the microscope was determined both in the laboratory and *in situ*. Figure 78.25(a) shows a typical grating-dispersed image of an imploded hollow-shell target. The bright central peak is the overexposed image of the core (zeroth-order image), while the indicated lines are diffracted images of the core (±first-order images). The spectrum of the core emission, after correction for instrument response, is shown in Fig. 78.25(b) along with a model fit to the spectrum (thermal bremsstrahlung with absorption). (The details of this analysis will be described in the next section.) The crystal spectrometer consisted of an imaging slit in front of a diffraction crystal viewing the target. Diffracted x rays were recorded with DEF film as were the spectrally dispersed images from the

KB microscope. The emission from the implosion core was separated from the total flux by the narrow size of the imaging slit (~100 μm). The spectrometer was set to view a region of the spectrum from ~4 to 6 keV containing continuum emission from the targets. This was compared to the KB microscope–derived spectra on certain shots. A limited number of shots were taken with targets containing a Ti-doped layer, and in such cases the observed jump in the spectrum at the Ti K edge was used to infer the shell areal density.[15]

Primary neutron yield (D-D neutrons) was measured with an array of cross-calibrated scintillator detectors. Secondary neutron yield was measured with an 824 detector array of
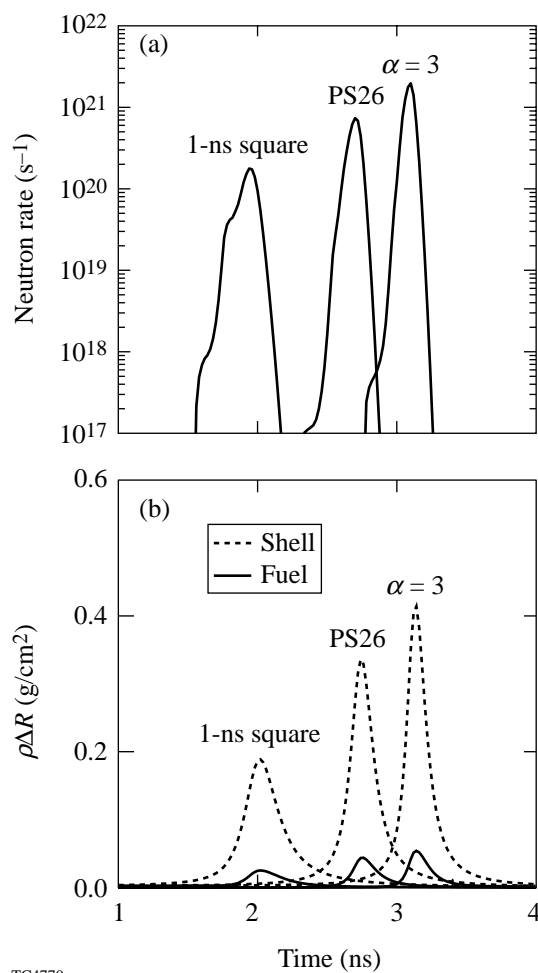
Figure 78.24
Simulations of the (a) D-D neutron-generation rate and (b) the fuel and shell areal densities as functions of time for the three pulse shapes. The targets were all assumed to be 20-μm-thick CH shells, filled with 3 atm of D^{3}He, imploded by a total energy of 25 kJ.
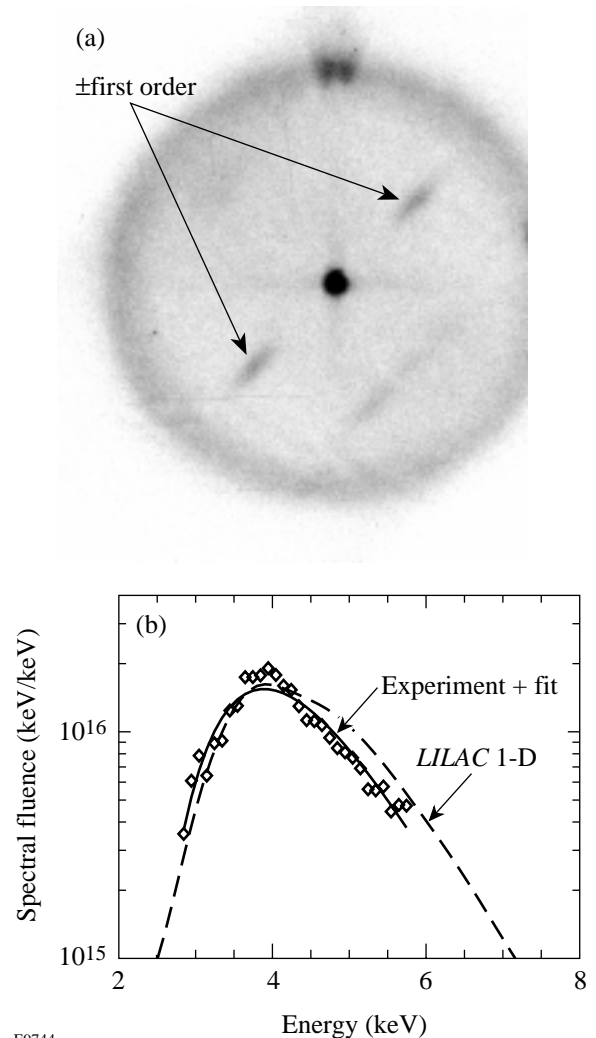
Figure 78.25
Grating-dispersed KB microscope image of OMEGA shot 9130 (see Table 78.IV): (a) the zeroth-order image with ±first-order diffracted images of the core (indicated), and (b) the core spectrum after correction for instrument response, along with 1-D (*LILAC*) simulations of the same.

scintillators, each of which records the neutron arrival time to an accuracy of ~0.5 ns, which translates into an accuracy in energy of ~0.5 MeV. This instrument, called MEDUSA (Multi-Element Detector Using a Scintillator Array),[16] allows for the determination of the much smaller secondary neutron yield (D-T neutrons) due to their earlier arrival time at the detector. Figure 78.26 shows an example spectrum from MEDUSA on a 20-μm-thick CD/CH shell imploded with a 1-ns square pulse and coherent beam illumination. The secondary neutron yield is clearly seen, appearing as the broad peak between 12 and 17 MeV. The integral of this peak is proportional to the secondary yield.

100
80
60
40
20
0

dN/dE (neutrons/channel)

OMEGA shot 9122

DD primaries

DT secondaries

0   5   10   15   20
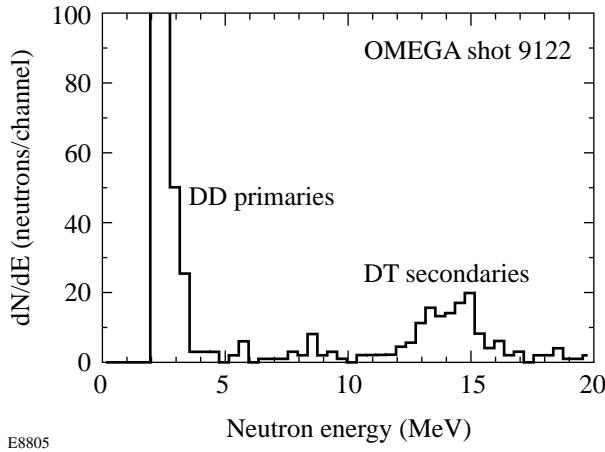
Neutron energy (MeV)

E8805

Figure 78.26
Example of the neutron spectrum emitted by a CD target as determined by MEDUSA. The neutrons with energies from 12 to 17 MeV are from DT fusion reactions generated by primary-fusion-product (secondary) tritons fusing with primary deuterons.

Results

Several combinations of shell thicknesses (CD/CH and CH only), fill gases, and pulse shapes were investigated. We present here a representative set from which x-ray and neutron spectral information was obtained. Table 78.IV is a sample of the target shot conditions and experimentally measured values. The conditions for each shot, illumination type, energy, D-D yield, D-T yield (where measured), kT_e, and ρR, along with *LILAC* predictions of these quantities, are grouped by type of pulse shape. The implosions were simulated with the one-dimensional hydrocode *LILAC*, which uses tabulated equation of state (SESAME),[17] flux-limited electron transport, and multi-group radiation transport using local thermodynamic equilibrium (LTE) opacities,[18] and inverse-bremsstrahlung-absorption energy deposition through a ray-tracing algorithm in the underdense plasma. A flux limiter of $f = 0.06$ with a

sharp cutoff was used. The primary fusion reaction products were transported using a multi-angle straight-line method, which also includes the production of neutrons from the secondary D-T reactions. The detailed space-resolved x-ray spectra generated for comparison with the observations were calculated with a postprocessor.

As shown in previous works,[14,19] the x-ray spectrum emitted by an undoped polymer shell can, to a good approximation, be represented by

$$I_x = I_{\text{hot}} \, e^{-E/kT_{\text{hot}}} \, e^{-\langle \mu(E)\rho R \rangle_{\text{shell}}} , \qquad (1)$$

where I_{hot} is the intensity of the thermal bremsstrahlung emission from the core region, which has a characteristic temperature kT_{hot}. Absorption will occur in the shell as x rays exit the core through the surrounding colder shell whose optical depth $\tau = \langle \mu(E)\rho R \rangle$, where $\mu(E)$ is the energy-dependent mass absorption coefficient and ρR is the areal density (the brackets indicate an average over the shell). To a good approximation μ is given by

$$\mu = 1.9 \times 10^3 \frac{1}{E^3} g(\rho, kT) \quad (\text{cm}^2/\text{g}), \qquad (2)$$

where E is in keV and $g \leq 1$. Using this approximation, a lower limit on ρR_{shell} can be determined by fitting the observed spectrum to I_X with the optical depth given by

$$\tau = 1.9 \times 10^3 \frac{\rho R_{\text{cold}}}{E^3} , \qquad (3)$$

where ρR_{cold} is the areal density of the cold shell material and, therefore, a lower limit on the total ρR_{shell}. Both ρR_{cold} and the average electron temperature kT_e are determined by fitting Eq. (1) to the observed spectrum.

The combined measurements of the primary neutron yield from the D-D reaction and the secondary neutron yield from the D-T reaction allow us to estimate the areal density of the deuterium-bearing shell material ρR_{CD} using the following:

$$\rho R_{\text{CD}} \geq \left[\frac{Y_{\text{DT}}}{Y_{\text{DD}}} \middle/ 4.3 \times 10^{-2} \right] \left(\text{g}/\text{cm}^2 \right), \qquad (4)$$

where we have used the results of Azechi, Cable, and Stapf[20] scaled to CD (which has a 6:1 ratio of carbon to deuterium

mass) and we have taken the maximum calculated ratio as a function of temperature as the limit given above. Since the range of the primary 1-MeV tritons may be smaller than the total areal density of the CD layer ρR_{CD} and since ρR_{CD} is less than the total ρR_{shell}, this value again places a lower limit on ρR_{shell}.

Figure 78.27 shows the measurements of kT_e and *LILAC* predictions of these values for the voided targets imploded by 1-ns square pulses. (The values obtained from simulations are averaged over the stagnation, as is the case for all comparisons to measurements that follow. The simulated x-ray measurements are weighted by emitted x-ray intensity, whereas the simulated neutron measurements are values averaged over the time of neutron emission.) The measured values of kT_e show little discernible difference for the three illumination conditions. (Note that slightly less energy was used to implode the targets with DPP+SSD illumination.) The thinnest-shell

targets have measured kT_e values that are slightly lower than the predicted values.

Figure 78.28 shows the measured values of ρR_{cold} from the x-ray spectra for 1-ns-square-pulse illumination. Here we have included both the voided CD/CH shells and the 3-atm-filled CH shells. The higher measured values of ρR_{cold} for the thicker-shell targets are evident, following the trend of the simulations, which is expected since the implosion cores of thicker targets reach a lower temperature. (Therefore the shell material is less stripped and can more heavily absorb the continuum emission from the core.) The significantly lower values of ρR_{cold} for the DPP-only cases are also noticeable. This difference is largest for the 3-atm-filled CH targets pointing to the gas–shell interface as a source of disruption to the symmetry of the implosion. The differences between DPP+SSD and DPP-only illumination for gas-filled targets are further apparent when one compares their spectra

Table 78.IV: Measured and simulated values for a representative sample of voided CD/CH target experiments. The numbered columns contain the following: (1) pulse type, (2) beam-smoothing condition, (3) shell thickness, (4) energy on target, (5) the measured D-D neutron yield [Y_n (D-D)], (6) error of measurement of Y_n (D-D), (7) the measured D-T neutron yield [Y_n (D-T)], (8) error of measured Y_n (D-T), (9) the CD layer areal density ρR_{CD} determined from Eq. (4), (10) error of ρR_{CD} value, (11) *LILAC*-predicted value of Y_n (D-D), (12) YOC (D-D), the ratio of the measured-to-predicted values of Y_n (D-D), (13) *LILAC*-predicted value of Y_n (D-T), (14) *LILAC*-predicted value of ρR_{CD}, (15) *LILAC*-predicted

| Shot	1 Pulse Type	2 Illumination Condition	3 CD+CH (μm)	4 Energy (kJ)	5 Y_n(D-D)	6 Y_n(D-D) error	7 Y_n(D-T)	8 Y_n(D-T) error	9 ρR_{MED} (mg/cm²)	10 ρR_{MED} error (mg/cm²)	11 Y_n(D-D) 1-D	12 YOC (D-D)
7817	1-ns sq	Coherent	31.8	26.2	2.3(8)	6.7(6)					4.9(8)	0.47
9130	1-ns sq	Coherent	39.4	28.4	7.4(7)	2.5(6)					1.1(8)	0.66
9266	1-ns sq	Coherent	25.6	29.2	5.4(8)	7.0(6)					6.1 (9)	0.09
9267	1-ns sq	Coherent	34.4	30.2	1.6(8)	3.7(6)					5.2(8)	0.31
14010	1-ns sq	DPP's only	21.2	28.0	1.4(9)	3.2(7)	4.1(6)	2.6(5)	69.0	4.8	1.7(10)	0.08
14012	1-ns sq	DPP's only	31.0	27.2	2.5(8)	1.4(7)	5.0(5)	8.6(4)	45.4	8.3	5.9(8)	0.43
11561	1-ns sq	DPP's + SSD	19.9	27.3	2.6(9)	2.0(8)	7.3(6)	3.7(5)	64.9	6.1	1.8(10)	0.15
11562	1-ns sq	DPP's + SSD	30.9	28.3	2.5(8)	6.4(7)	4.6(5)	8.3(4)	42.2	13.2	5.7(8)	0.44
11576	1-ns sq	DPP's + SSD	38.9	27.7	1.4(8)	1.6(6)	1.8(5)	5.1(4)	30.1	8.7	6.7(7)	2.03
12538	1-ns sq	DPP's + SSD	21.1	24.0	1.4(9)	5.5(7)	6.0(6)	3.3(5)	102.3	7.0	5.9(9)	0.23
12548	$\alpha = 3$	DPP's + SSD	21.1	20.6	1.7(8)	2.6(6)	7.2(4)	3.2(4)	9.7	4.4	8.6(9)	0.02
12549	$\alpha = 3$	DPP's + SSD	26.9	21.2	1.1(8)	2.0(6)	5.7(4)	2.9(4)	12.5	6.3	1.3(9)	0.08
12551	$\alpha = 3$	DPP's + SSD	30.8	21.0	4.4(7)	1.3(6)	2.8(4)	2.0(4)	15.0	10.6	3.8(8)	0.12
12562	PS26	DPP's + SSD	21.3	19.6	7.8(7)	1.3(7)	1.1(5)	4.1(4)	34.4	13.5	1.0(10)	0.01
12563	PS26	DPP's + SSD	26.9	19.8	6.5(7)	1.2(7)	1.4(5)	4.5(4)	50.9	18.6	3.0(9)	0.02
12567	PS26	DPP's + SSD	30.7	20.0	7.8(7)	1.3(7)	2.9(5)	6.4(4)	85.6	24.0	1.7(9)	0.05
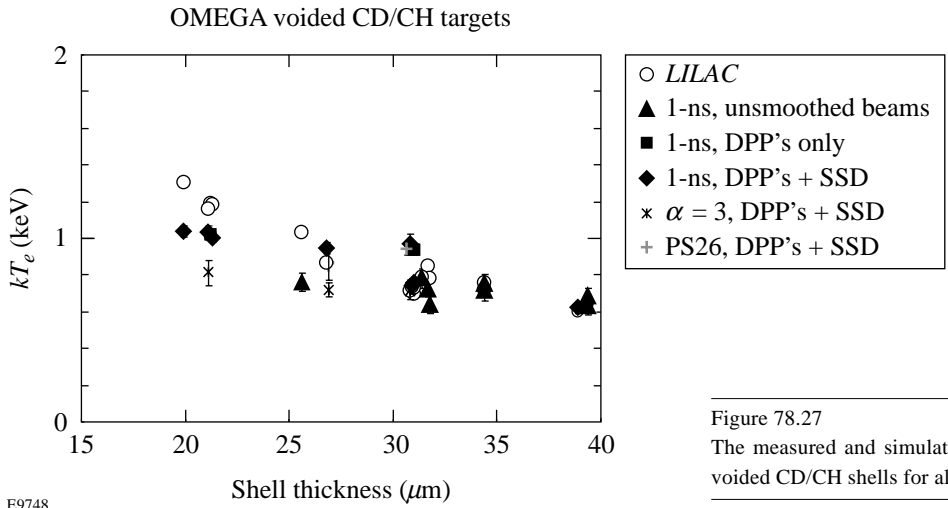
Figure 78.27
The measured and simulated values of kT_e versus shell thickness for the voided CD/CH shells for all pulse shapes.

value of ρR_{shell} averaged over the time of neutron production, (16) *LILAC*-predicted value of the ion temperature (kT_i) averaged over the time of neutron production, (17) the x-ray-spectrum determined electron temperature (kT_e), (18) error of (kT_e), (19) the *LILAC*-predicted value of the kT_e, as would be determined from the x-ray spectrum, (20) the x-ray spectrum determined cold shell density (ρR_{cold}), (21) error of ρR_{cold}, (22) the *LILAC*-predicted value of ρR_{cold}, (23) the inferred shell areal density (ρR_{shell}), and (24) error of experimentally determined value of ρR_{shell}. [*Numbers in ( ) indicate the power of 10; i.e., 2.3(8) = 2.3×10^8].

13	14	15	16	17	18	19	20	21	22	23	24
Y_n(DT) 1-D	ρR_{MED} 1-D (mg/cm^2)	$<\rho R>_n$ 1-D (mg/cm^2)	$<kT_i>_n$ 1-D (keV)	kT_e (KB) (keV)	kT_e error (keV)	kT_e 1-D (keV)	ρR_{cold} (KB) (mg/cm^2)	ρR_{cold} error (mg/cm^2)	ρR_{cold} 1-D (mg/cm^2)	ρR_{shell} (KB) (mg/cm^2)	ρR_{shell} error (mg/cm^2)
1.3(6)		199	0.67	0.64	0.05	0.78	31	6	67	93	18
2.3(5)		170	0.58	0.68	0.05	0.65	61	7	74	140	16
2.6(7)		268	1.03	0.76	0.05	1.03	26	5	76	92	18
1.3(7)		196	0.68	0.71	0.05	0.72	38	6	74	100	16
9.0(7)	127.3	320	1.19	1.02	0.03	1.19	8	1	89	29	4
1.5(6)	58.6	196	0.68	0.94	0.03	0.73	22	1	69	63	3
9.7(7)	128.6	312	1.22	1.04	0.03	1.30	13	1	58	71	5
1.4(6)	59.1	201	0.68	0.74	0.04	0.73	27	3	70	78	9
1.3(5)	43.5	165	0.54	0.62	0.03	0.60	52	7	76	113	15
2.4(7)	96.2	329	1.02	1.03	0.05	1.16	16	3	38	139	22
4.3(7)	117.4	323	1.11	0.81	0.07	1.19	0	3	111	0	
4.0(6)	72.9	254	0.75	0.72	0.04	0.85	16	2	91	45	6
9.3(5)	56.9	224	0.61	0.72	0.05	0.66	22	3	92	54	7
5.4(7)	123.1	346	1.25			1.30			150		
1.2(7)	95.1	338	0.88	0.86	0.09	0.89	29	4	179	54	7
6.6(6)	88.2	368	0.80	0.94	0.03	0.85	42	2	209	74	4

[shown for two different shell thicknesses, 20 and 25 μm, in Figs. 78.29(a) and 78.29(b)]. The low-energy portions of the spectra exhibit a marked difference indicative of lower compression for the DPP-only cases, despite the fact that the high-energy portions of the spectra are nearly identical. This indicates that conditions in the highest-temperature regions of the implosion (i.e., the gas-filled cores and inner edge of the shell) were unaffected by the different conditions obtained in the shell. Additionally, differences between the three pulse shapes are seen in the measured values of ρR_{cold} (Fig. 78.30). The shaped-pulse implosions have lower measured shell areal densities than with a square pulse (see Fig. 78.28), with the highest-contrast-pulse-shape implosions ($\alpha = 3$) having the lowest values. All DPP-only cases are lower than the comparison DPP+SSD cases.

The measured primary (D-D) neutron yields of the voided CD/CH targets for all pulse shapes are shown in Fig. 78.31(a). The ratios of the measured primary yield to the *LILAC*-calculated yield (normalized yield) are shown in Fig. 78.31(b). The primary yields obtained from implosions with 1-ns-square-pulse illumination follow a fairly well-defined trend with the highest yields obtained for the thinnest shells (highest calculated central temperatures and areal densities). Little difference is seen for the three uniformity conditions, indicative of the insensitivity of the shell/void interface to the illumination conditions employed. Lower absolute yields were obtained for the shaped-pulse implosions [Fig. 78.31(a)]; although, due to current OMEGA laser operation conditions, the maximum on-target energy is less for the shaped pulses (~21 kJ). Nevertheless, lower normalized yields were obtained for the
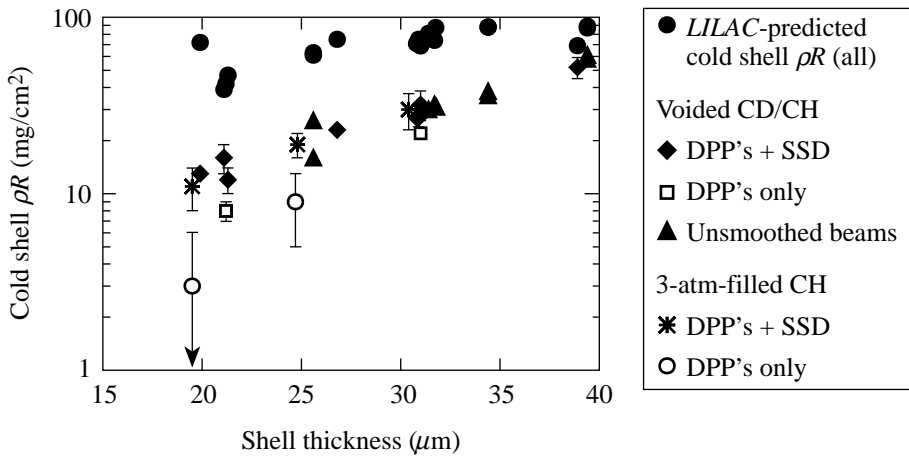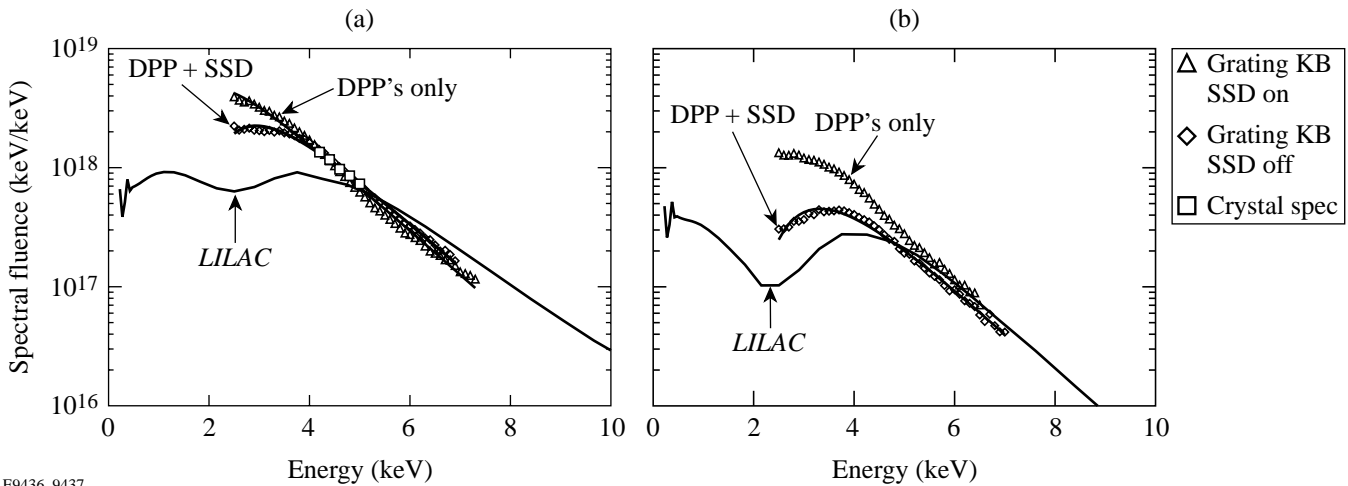

Figure 78.28
The measured values of ρR_{cold} for the voided CD/CH and 3-atm-filled CH targets from shots with 1-ns-square-pulse illumination. Cases of all three laser-beam conditions are shown: unsmoothed beams, DPP only, and DPP+SSD smoothed beams. The values of ρR_{cold} expected from *LILAC* simulations are also shown.
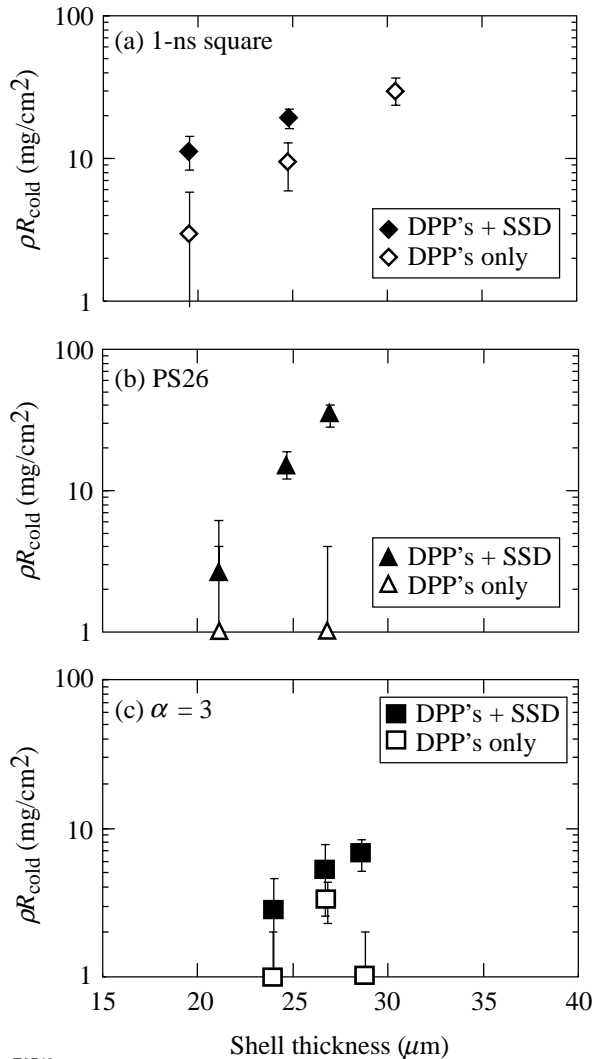

Figure 78.29
The measured and predicted core x-ray spectra from two DPP-only/DPP+SSD pairs of CH targets filled with 3 atm of D^{3}He and imploded with 1-ns square pulses: (a) a 20-μm-thick pair and (b) a 25-μm-thick pair. Note the agreement between KB-microscope- and crystal-spectrometer-determined spectra in (a).

shaped pulses [Fig. 78.31(b)] with the lowest yield for the PS26 pulse shape.

Figures 78.32(a) and 78.32(b) show the measured primary and secondary neutron yields along with the *LILAC*-simulated yields for the voided CD/CH shells imploded with the 1-ns-pulse shape. Again the trend is to lower yields for thicker shells, with the measured yields for thicker shells closer to the simulated yields, indicating less disruption during implosion for the thicker shells. As discussed previously, a lower limit on ρR_{shell} is determined from the simultaneous measurements of primary (D-D) and secondary (D-T) neutron yield. Fig-

ure 78.33 shows the values so obtained for the voided CD/CH shells along with *LILAC* predictions of the measurements. The thinner targets have both higher measured and predicted ρR_{shell} values, opposite to the trend seen in the x-ray measurements, because of the larger range of tritons in the higher-temperature conditions, expected and obtained, for the thinner shells. Quite striking is the trend to lower ρR_{shell} for the thinner shells imploded with shaped pulses, which is lowest for the highest-contrast pulse shape ($\alpha = 3$). This again is indicative of shell disruption for the shaped-pulse implosions (resulting in lower apparent compression at the time of this measurement). The trend is similar to that seen for ρR_{shell} measurements obtained from the x-ray spectra (Fig. 78.29). The observed compression is less for the shaped-pulse implosions from both sets of measurements.

The combined measurements of ρR_{shell} from both the x-ray spectra and the primary-to-secondary-yield ratio for the voided targets are shown in Fig. 78.34. The dotted line and arrows indicate the lower limit on ρR_{shell} obtained from the
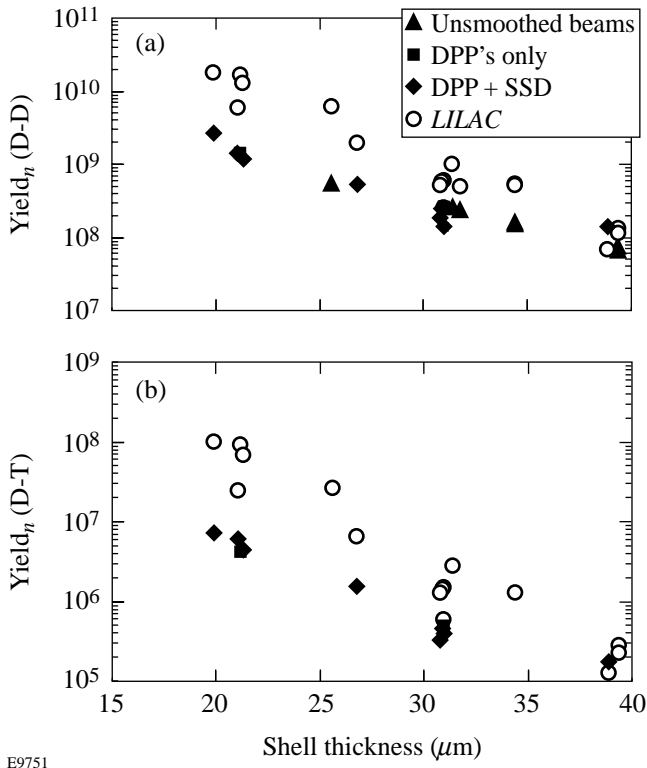

Figure 78.30

The measured values of ρR_{cold} for 3-atm-filled CH targets from shots with (a) 1-ns square, (b) PS26, and (c) $\alpha = 3$ pulse illumination.
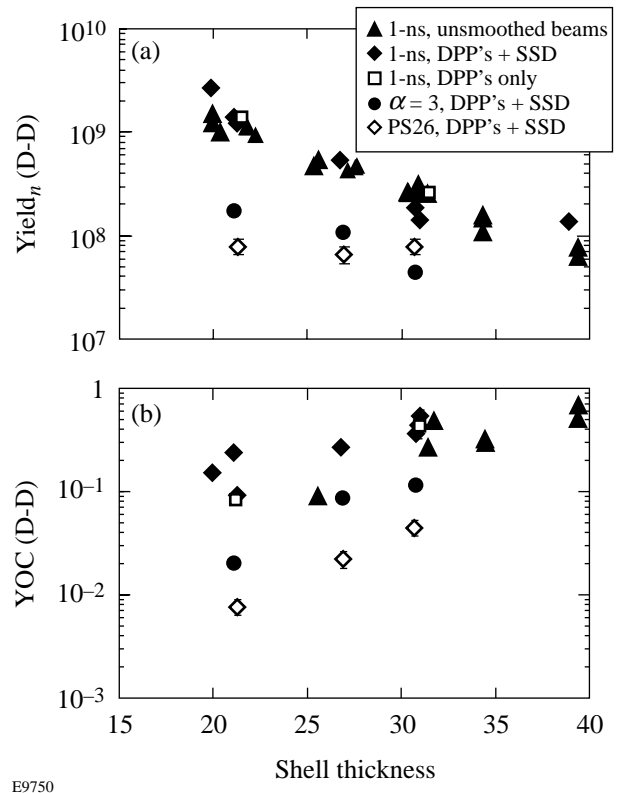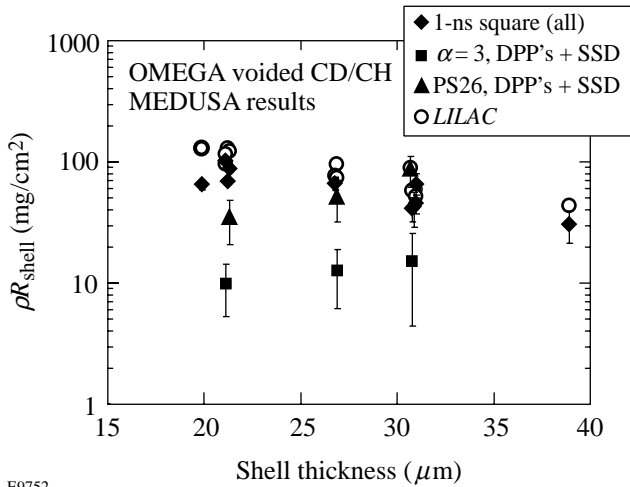

Figure 78.31

Measurements of the primary (D-D) neutron yield from voided CD/CH shells for all three pulse shapes versus shell thickness: (a) the absolute measured yield and (b) the normalized yield (measured/calculated).

E9751

Figure 78.32

Measurements of (a) primary (D-D) and (b) secondary (D-T) neutron yield from voided CD/CH shells imploded with 1-ns square pulses from the three beam-uniformity cases versus shell thickness. *LILAC* predictions of the measurements are also shown.
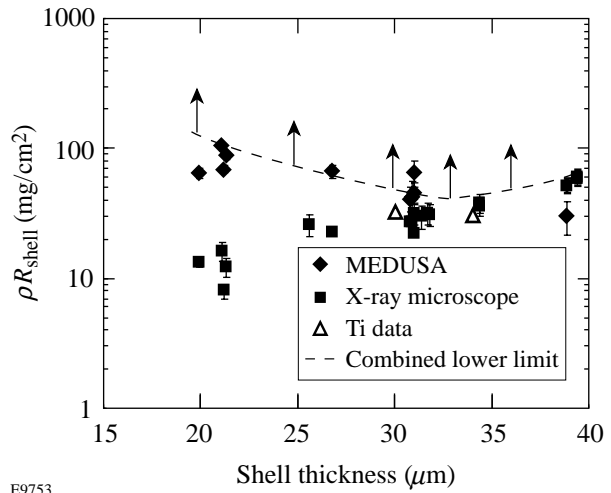
combined measurements. The estimates of ρR_{shell} obtained from Ti-doped shells as reported by Yaakobi and Marshall[15] are also shown (these values are lower limits as well). Both sets taken together indicate that ρR_{shell} in excess of ~60 mg/cm^2 has been obtained in every case. Assuming that the ionization state of the target is properly predicted by the hydrocode simulations, an estimate of the full ρR_{shell} can be determined by correcting the x-ray measurements of ρR_{cold} by the predicted ionization fraction. Values so determined are shown in Fig. 78.35. The estimated x-ray–averaged ρR_{shell} ranges from ~60 to 130 mg/cm^2.

Conclusions

In conclusion, we have performed experiments on hollow-shell (CD/CH and CH only), evacuated or low-pressure-filled (3-atm) targets with the OMEGA laser system demonstrating compression of the shell material (surrogate-cryogenic fuel) to areal densities of ~60 to 130 mg/cm^2. The survey of various implosion conditions (unsmoothed to smoothed beams; high-intensity, short-pulse shapes to ramped-intensity, longer-pulse shapes) has yielded information about the target performance as a function of illumination (laser drive) relevant to cryogenic-target experiments to follow. Specifically for a 1-ns square pulse and evacuated targets, the primary neutron yield from the core is not greatly affected by the differences in illumination uniformity at current levels; however, both the illumination uniformity and the initial shell thickness affect the final shell areal density. The thicker-shell targets compress to

E9752

Figure 78.33

The measured lower limits on ρR_{shell} of the voided CD/CH shells from MEDUSA measurements versus shell thickness for the various cases of pulse shape and beam uniformity. The values expected from *LILAC* simulations are shown for comparison.

E9753

Figure 78.34

Combined upper-limit values on ρR_{shell} of the voided CD/CH shells imploded by 1-ns square pulses determined from both the x-ray and neutron spectra. Additional measurements determined from Ti-doped targets are shown to give consistent lower limits.
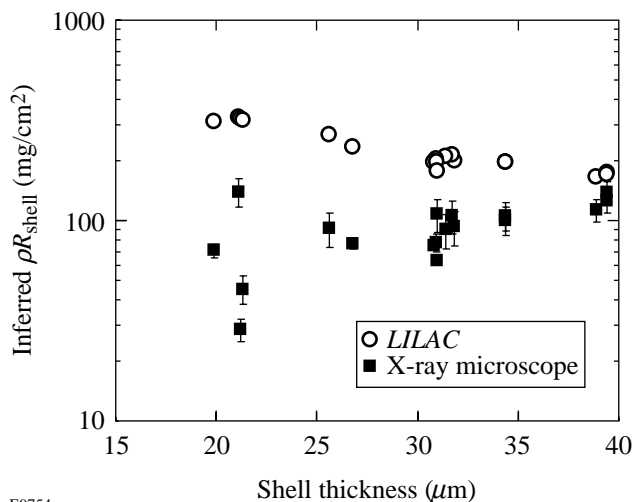
E9754

Figure 78.35
Estimates of ρR_{shell} for the voided CD/CH shells imploded by 1-ns square pulses determined from the lower limits (ρR_{cold}) given in Fig. 78.28. The values are determined assuming the ionization fraction predicted by *LILAC*.

areal densities as high as the thinner shells (at least as inferred by currently available techniques) despite the lower specific energy applied to the target, which implies that they are less affected by instabilities. All targets perform more poorly (lower yield, less compression) when imploded by the longer, shaped pulses because they have higher levels of laser imprint and lower ablative stabilization, which leads to large growth rates; thus, shaped-pulse implosions place more stringent requirements on power balance and initial target and illumination uniformity. For all pulse shapes, the gas-filled targets have the most significant increase in measured shell areal density when SSD is turned on (compared to DPP's only). This demonstrates the benefit of SSD in reducing the added instabilities that occur at the gas–shell interface. It is expected that as more-uniform illumination conditions are obtained, the thinner targets will outperform the thicker targets. This would be evidenced in higher neutron yields and higher areal densities as measured by x-ray and neutron spectral diagnostics.

ACKNOWLEDGMENT

REFERENCES

1. T. R. Boehly, D. L. Brown, R. S. Craxton, R. L. Keck, J. P. Knauer, J. H. Kelly, T. J. Kessler, S. A. Kumpan, S. J. Loucks, S. A. Letzring, F. J. Marshall, R. L. McCrory, S. F. B. Morse, W. Seka, J. M. Soures, and C. P. Verdon, Opt. Commun. **133**, 495 (1997).

2. T. J. Murphy, J. M. Wallace, N. D. Delamater, C. W. Barnes, P. Gobby, A. A. Hauer, E. Lindman, G. Magelssen, J. B. Moore, J. A. Oertel, R. Watt, O. L. Landen, P. Amendt, M. Cable, C. Decker, B. A. Hammel, J. A. Koch, L. J. Suter, R. E. Turner, R. J. Wallace, F. J. Marshall, D. Bradley, R. S. Craxton, R. Keck, J. P. Knauer, R. Kremens, and J. D. Schnittman, Phys. Rev. Lett. **81**, 108 (1998).

3. J. D. Kilkenny, in *Current Trends in International Fusion Research*, edited by E. Panarella (Plenum Press, New York, 1997), pp. 295–296.

4. M. D. Rosen, Phys. Plasmas **3**, 1803 (1996).

5. J. T. Hunt *et al.*, Lawrence Livermore National Laboratory, Livermore, CA, UCRL-JC-117399 (1994).

6. J. Nuckolls *et al.*, Nature **239**, 139 (1972).

7. R. E. Kidder, Nucl. Fusion **19**, 223 (1979).

8. J. M. Soures, R. L. McCrory, C. P. Verdon, A. Babushkin, R. E. Bahr, T. R. Boehly, R. Boni, D. K. Bradley, D. L. Brown, R. S. Craxton, J. A. Delettrez, W. R. Donaldson, R. Epstein, P. A. Jaanimagi, S. D. Jacobs, K. Kearney, R. L. Keck, J. H. Kelly, T. J. Kessler, R. L. Kremens, J. P. Knauer, S. A. Kumpan, S. A. Letzring, D. J. Lonobile, S. J. Loucks, L. D. Lund, F. J. Marshall, P. W. McKenty, D. D. Meyerhofer, S. F. B. Morse, A. Okishev, S. Papernov, G. Pien, W. Seka, R. Short, M. J. Shoup III, M. Skeldon, S. Skupsky, A. W. Schmid, D. J. Smith, S. Swales, M. Wittman, and B. Yaakobi, Phys. Plasmas **3**, 2108 (1996).

9. D. K. Bradley, J. A. Delettrez, R. Epstein, R. P. J. Town, C. P. Verdon, B. Yaakobi, S. Regan, F. J. Marshall, T. R. Boehly, J. P. Knauer, D. D. Meyerhofer, V. A. Smalyuk, W. Seka, D. A. Haynes, Jr., M. Gunderson, G. Junkel, C. F. Hooper, Jr., P. M. Bell, T. J. Ognibene, and R. A. Lerche, Phys. Plasmas **5**, 1870 (1998).

10. P. C. Souers, *Hydrogen Properties for Fusion Energy* (University of California Press, Berkeley, 1986).

11. The Department of Energy's designated target supplier for the U.S. ICF Program is General Atomics, Inc., San Diego, CA 92121-1194.

12. T. J. Kessler, Y. Lin, L. S. Iwan, W. P. Castle, C. Kellogg, J. Barone, E. Kowaluk, A. W. Schmid, K. L. Marshall, D. J. Smith, A. L. Rigatti, J. Warner, and A. R. Staley, in *Solid State Lasers for Application to Inertial Confinement Fusion*, edited by M. L. André (SPIE, Bellingham, WA, 1997), Vol. 3047, pp. 272–281.

13. S. Skupsky, R. W. Short, T. Kessler, R. S. Craxton, S. Letzring, and J. M. Soures, J. Appl. Phys. **66**, 3456 (1989).

14. F. J. Marshall, J. A. Delettrez, R. Epstein, and B. Yaakobi, Phys. Rev. E **49**, 4381 (1994).

15. B. Yaakobi, R. Epstein, and F. J. Marshall, Phys. Rev. A **44**, 8429 (1991).

16. J. P. Knauer, R. L. Kremens, M. A. Russotto, and S. Tudman, Rev. Sci. Instrum. **66**, 926 (1995).

17. B. I. Bennett *et al*., Los Alamos National Laboratory Report LA-7130 (1978).

18. W. F. Huebner *et al.*, Los Alamos National Laboratory Report LA-6760-M (1977).

19. B. Yaakobi and F. J. Marshall, J. Quant. Spectrosc. Radiat. Transfer **61**, 465 (1999).

20. H. Azechi, M. D. Cable, and R. O. Stapf, Laser Part. Beams **9**, 119 (1991).